Analysis and Design of High-Misalignment-Tolerant Compensation Topologies With Constant-Current or Constant-Voltage Output for IPT Systems

Jianwei Mai, *Student Member, IEEE*, Yijie Wang, *Senior Member, IEEE*, Yousu Yao, *Member, IEEE*, and Dianguo Xu, *Fellow, IEEE*

***Abstract*—The capability of misalignment tolerance is vital for an inductive power transfer system. The conditions satisfied by the high-misalignment-tolerant compensation topology are proposed in the article. It is proven that all compensation topologies with secondary parallel compensation component have a strong capability of misalignment tolerance if the parameters of the compensation circuit are properly designed. And, their misalignment-tolerant capability was analyzed. The impedance characteristics of the simple S/T compensation topology are analyzed. Two prototypes of approximately 300 W used S/SP (primary series, secondary series–parallel) compensation topology with strong misalignment tolerance were designed to verify the system performance. They have the characteristics of constant-voltage and constant-current output, respectively.**

***Index Terms*—Inductive power transfer (IPT), input impedance angle, misalignment tolerance, output voltage fluctuation range, S/SP compensation topology.**

I. Introduction

As a method alternative to traditional physical contact, inductive power transfer (IPT) have been paid more and more attention from consumers and research communities. It has good application prospects in the fields of electric vehicles, consumer electronics, biomedicine, and other industrial areas due to its excellent characteristics of avoidance of bulky cables, availability of galvanic isolation, more degrees of operational freedom, weather proofing, low maintenance, and higher safety [1]–[6]. However, the weak space freedom still hinder its development, more research work is required to increase misalignment tolerance.

The researchers have proposed many methods to improve misalignment tolerance. Four compensation topologies, including SS (primary series, secondary series) [7], SP/S (primary series–parallel, secondary series) [8], T/S (primary T-type network, secondary series) [9], and S/SP(primary series, secondary series–parallel) [10], that transfer rated power even with misalignment have been proposed in past several years. However, there are very few applications that require constant output power. Conversely, constant voltage (CV) or constant current (CC) are more popular.

Many compensation topologies with zero input impedance angle providing CV or CC have been proposed, such as four basic topologies, including S/S, S/P, PS, PP, LCC/S [11], LC/S [12], LCC/LCC [13]–[14], S/SP [15]–[18]. "S," "P," "L," and "C" in these compensation topology names denote "series," "parallel," "inductor," and "capacitor," respectively. The primary compensation structure is indicated on the left side of the slash symbol "/," and secondary compensation structure is indicated on the right side. In addition, the higher order compensation for inductive-power-transfer converters with CV or CC output is researched in [19]. Moreover, more attention is paid in [20]–[22] to combine topologies with CC and CV outputs for battery charging. However, these compensation topologies operating in resonance do not have the capability of misalignment tolerance.

Some researchers pay more and more attention to the compensation topologies with high-misalignment tolerance and CV or CC. In [15], an S/SP (primary series, secondary series parallel) compensation topology with high misalignment tolerance is proposed to provide a constant output voltage. But its application is very limited, if the self-inductance of the loosely coupled transformer (LCT) do not reduce drastically as the decrease of coupled coefficient, the strong misalignment-tolerant capacity of the LCT will disappear. Therefore, its application is mostly the change of breath in a close range.

In order to solve the problems in [15], the work in [18] improved the parameter design to reduce the dependence of the compensation topology on LCT. The design method of [18] has no contradiction with the design method of this article. However, the work in [18] only optimizes the S/SP compensation topology with CV output. And, it only compensates for the leakage inductance of the loosely coupled transformer, which results in the output voltage not being adjustable.

In [23], a PS/S (primary parallel–series secondary series) compensation topology with constant output current and high misalignment tolerance is put forward, However, due to the limitation of the misalignment-tolerant capability of the

Manuscript received March 9, 2020; revised June 18, 2020; accepted July 29, 2020. Date of publication August 6, 2020; date of current version October 30, 2020. This work was supported in part by the National Natural Science Foundation of China under Grant 51922033, and in part by the Power Electronics Science and Education Development Program of Delta Group. Recommended for publication by Associate Editor J.-i. Itoh. *(Corresponding author: Yijie Wang.)*

The authors are with the School of Electrical Engineering and Automation, Harbin Institute of Technology, Harbin 150001, China (e-mail: 407031956@qq.com; wangyijie@hit.edu.cn; yaoyousu@163.com; xudiang@hit.edu.cn).

Color versions of one or more of the figures in this article are available online at https://ieeexplore.ieee.org.

Digital Object Identifier 10.1109/TPEL.2020.3014687

compensation topology, its output current fluctuates greatly. In addition, an S/CLC (primary series, secondary capacitor–inductor–capacitor) compensation topology with wide misalignment is proposed in [24]. But its load variation range is too small. And there are many compensation components used. Although the coupling coefficient is as high as 0.4, the efficiency is only 88.2%. Moreover, the hybrid topology is applied to the IPT system in order to obtain excellent misalignment tolerance [25]–[27]. However, it caused the system to become very complicated. At least eight compensation components and four coils that make up the LCT are required. On the other hand, the hybrid topology requires that the cross coupling of the LCTs used in the two sets of compensation topologies be as small as possible, which limits the misalignment direction of the LCT, and often has the capability of misalignment tolerance in the *x*-direction on a plane. Therefore, the application of hybrid topology is limited.

In the past, the study of compensation topology with misalignment tolerance can be divided into three categories. The first is the compensation topology with constant power (CP) output, such as [7]–[10]. The second is the compensation topology that cooperates with a specific LCT, and its misalignment direction is limited, such as single compensation topology [15] and hybrid topology [25]–[27]. The third is the compensation topology with CV or CC output, which does not require a specific LCT, such as [18], [22], and [23]. However, there are many compensation topologies with strong misalignment tolerance that have not yet been discovered. They are found and analyzed in this article.

A new method that designs the parameters of compensation topologies with high misalignment tolerance is proposed in the article. It is proven that all compensation topologies with secondary parallel compensation component have a strong capability of misalignment tolerance if the parameters of the compensation circuit are properly designed. Therefore, a family of compensation topologies with strong misalignment tolerances is proposed, such as S/P, S/SP, S/PS S/SPS, PS/SP, SPS/SP, and SPS/SPS compensation topologies. Their misalignment-tolerant capability was analyzed in this article. After analysis, they have the same misalignment tolerance. The impedance characteristics of the simple S/T compensation topology are analyzed to help the system implement ZVS. Two prototypes of approximately 300 W with S/SP (primary series, secondary series–parallel) compensation topology were designed to verify the system performance. They have the characteristics of CV and CC output, respectively. Their highest dc–dc efficiency is 94.7% and 94.8% respectively.

II. Analysis of Two-Port Network With High Misalignment Tolerance

In many applications, the primary coil always moves relative to the secondary coil. Therefore, the coupling coefficient of the LCT maybe change during the course of work, the compensation topologies necessitates good tolerance to high misalignment.

To facilitate the analysis, we simplify the IPT converter as a two-port network. The compensation network of the IPT system can be divided into two parts, including A_P and A_S, as shown in Fig. 1.

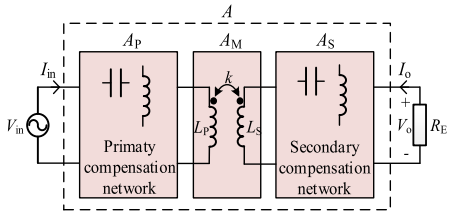

Fig. 1. Schematic of an IPT system as a two-port network.

Where $V_{\rm in}$ is a pure sinusoidal ac voltage source and R_E is the equivalent load. $L_{\rm P}$ and $L_{\rm S}$ are the self-inductances of the primary and secondary coupling coils, respectively. k is the coupling coefficient of the loosely coupled transformer (LCT). $I_{\rm in}$ and $I_{\rm o}$ are, respectively, the current of the voltage source and the current absorbed by R_E. $A_{\rm P}$, $A_{\rm M}$, and $A_{\rm S}$ are the transmission matrices of the primary compensation network, the LCT, and the secondary compensation network, respectively. A is the transmission matrix of the IPT converter. Hence

$$\begin{bmatrix} I_{\rm in} \\ V_{\rm in} \end{bmatrix} = A \begin{bmatrix} -I_{\rm o} \\ V_{\rm o} \end{bmatrix} = \begin{bmatrix} a_{11} & a_{12} \\ a_{21} & a_{22} \end{bmatrix} \begin{bmatrix} -I_{\rm o} \\ V_{\rm o} \end{bmatrix} \tag{1}$$

$$A = A_{\rm P} A_{\rm M} A_{\rm S} \tag{2}$$

$$a_{11}a_{22} - a_{21}a_{12} = 1. \tag{3}$$

Obviously, $V_{\rm o} = -I_{\rm o}R_{\rm E}$. The transfer functions for voltage ratio (voltage-controlled voltage source) E, transconductance (voltage-controlled current source) G, and input impedance $Z_{\rm in}$ shown as follows have been discussed in [19]

$$E = \frac{V_O}{V_{\rm in}} = \frac{R_{\rm E}}{a_{22}R_{\rm E} + a_{21}} \tag{4}$$

$$G = \frac{-I_O}{V_{\rm in}} = \frac{1}{a_{22}R_{\rm E} + a_{21}} \tag{5}$$

$$Z_{\rm in} = \frac{V_{\rm in}}{I_{\rm in}} = \frac{a_{22}R_{\rm E} + a_{21}}{a_{12}R_{\rm E} + a_{11}}. \tag{6}$$

To simplify the analysis, the parasitic resistance of the compensation component and transformer is ignored, a_{21} and a_{12} are pure imaginary number, and a_{11} and a_{22} are pure real number. When $a_{21} = 0$ or $a_{22} = 0$ at the designed coupling coefficient k_0, load-independent CV or CC output can be achieved. However, the constant CV or CC output of the IPT converter may be destroyed if the coupling coefficient fluctuates. Without changing the load-independent CV or CC output, the coupling-independent CV or CC output at the designed coupling coefficient is desired. The sensitivity of the voltage ratio E and transconductance G with respect to k can be calculated as follows.

For CV mode

$$\frac{\delta E}{\delta k} = -R_E \frac{R_E \frac{\delta a_{22}}{\delta k} + \frac{\delta a_{21}}{\delta k}}{\left(a_{22}R_E + a_{21}\right)^2}. \tag{7}$$

For CC mode

$$\frac{\delta G}{\delta k} = -\frac{R_{\rm E} \frac{\delta a_{22}}{\delta k} + \frac{\delta a_{21}}{\delta k}}{\left(a_{22}R_{\rm E} + a_{21}\right)^2}. \tag{8}$$

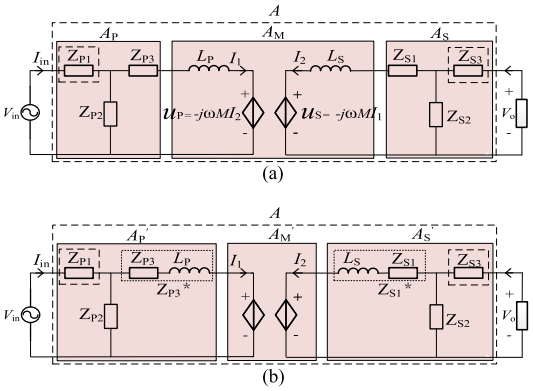

Fig. 2. Equivalent circuit of the IPT converter. (a) Equivalent circuit of the IPT converter. (b) Equivalent circuit of the IPT improved converter.

Actually, as long as $|E|$ is substantially constant when the coupling coefficient fluctuates, the CV or CC output is independent of the coupling. Since E is pure real number and G is pure imaginary number, the load-independent and coupling-independent CV or CC output at the designed coupling coefficient k_0 can be achieved when the real part of (7) or the imaginary part (8) is zero. Therefore, the conditions of load-independent and coupling-independent CV or CC output at the designed coupling coefficient k_0 is as follows.

For CV mode

$$\begin{cases} a_{21} = 0 \\ \frac{\delta a_{22}}{\delta k} = 0. \end{cases} \tag{9}$$

For CC mode

$$\begin{cases} \frac{\delta a_{21}}{\delta k} = 0 \\ a_{22} = 0. \end{cases} \tag{10}$$

III. High Misalignment Tolerant Compensation Design

Based on the reciprocity principle, a complex two-port passive linear network can be replaced by a T-type network. The LCT can be replaced by a model with controlled current source. The equivalent circuit of the IPT converter is shown in Fig. 2(a). Zp_1, Zp_2, and Zp_3 are the impedance of the first, second, and third compensation elements of the primary compensation network, respectively. Zs_1, Zs_2, and Zs_3 are the impedance of the first, second, and third compensation elements of the secondary compensation network, respectively.

u_{P} and u_{S} are the instantaneous voltages of the primary and secondary controlled source, respectively. ω is the angular frequency, and M is the magnetic inductor. I_1 and I_2 are the currents of the L_{P} and L_{S}, respectively. Z'_{P3} and L_{P} are connected in series. To simplify the analysis, Z_{P3} and $\mathrm{j}\omega L_{\mathrm{P}}$ are replaced by Z'_{P3} and the equivalent circuit of the IPT converter can be improved, as shown in Fig. 2(b). A'_{P}, A'_{M}, and A'_{S} are the new transmission matrices of the primary compensation network, the controlled current source and the secondary compensation network, respectively. Hence

$$A = A'_{\mathrm{P}} A'_{\mathrm{M}} A_{\mathrm{S}}{}' \tag{11}$$

$$A'_{\mathrm{P}} = \begin{bmatrix} \frac{Z_{\mathrm{P2}}+Z'_{\mathrm{P3}}}{Z_{\mathrm{P2}}} & \frac{1}{Z_{\mathrm{P2}}} \\ \frac{Z_{\mathrm{P1}}Z_{\mathrm{P2}}+Z_{\mathrm{P2}}Z'_{\mathrm{P3}}+Z_{\mathrm{P1}}Z'_{\mathrm{P3}}}{Z_{\mathrm{P2}}} & \frac{Z_{\mathrm{P1}}+Z_{\mathrm{P2}}}{Z_{\mathrm{P2}}} \end{bmatrix} \tag{12}$$

$$A_M{}' = \begin{bmatrix} 0 & \frac{1}{j\omega M} \\ -j\omega M & 0 \end{bmatrix} \tag{13}$$

$$A_{\mathrm{S}}{}' = \begin{bmatrix} \frac{Z_{\mathrm{S2}}+Z_{\mathrm{S3}}}{Z_{\mathrm{S2}}} & \frac{1}{Z_{\mathrm{S2}}} \\ \frac{Z'_{\mathrm{S1}}Z_{\mathrm{S2}}+Z_{\mathrm{S2}}Z_{\mathrm{S3}}+Z'_{\mathrm{S1}}Z_{\mathrm{S3}}}{Z_{\mathrm{S2}}} & \frac{Z'_{\mathrm{S1}}+Z_{S2}}{Z_{\mathrm{S2}}} \end{bmatrix} \tag{14}$$

where $M = k\sqrt{L_{\mathrm{P}}L_{\mathrm{S}}}$. Substituting (12), (13), and (14) into (11), A can be calculated as (15), as shown at the bottom of this page. Observe (15), each element in the transfer matrix is in the form of tick function shown in (16). It can be divided into five cases, and the first case is $m = 0$ and $n = 0$

$$y = mx + \frac{n}{x}. \tag{16}$$

a_{21} and a_{22} are pure imaginary number and real number, respectively. Equation (17) can be supposed. n_{21}, m_{21}, n_{22} and m_{22} can be expressed as (18)

$$\begin{cases} a_{21} = j(m_{21}k + \frac{n_{21}}{k}) \\ a_{22} = m_{22}k + \frac{n_{22}}{k} \end{cases} \tag{17}$$

$$\begin{cases} m_{21} = -\omega\sqrt{L_{\mathrm{P}}L_{\mathrm{S}}}\frac{Z_{\mathrm{P1}}+Z_{\mathrm{P2}}}{Z_{\mathrm{P2}}}\frac{Z_{\mathrm{S2}}+Z_{\mathrm{S3}}}{Z_{\mathrm{S2}}} \\ n_{21} = \frac{Z_{\mathrm{P1}}Z_{\mathrm{P2}}+Z_{\mathrm{P1}}Z'_{\mathrm{P3}}+Z_{\mathrm{P2}}Z'_{\mathrm{P3}}}{Z_{\mathrm{P2}}} \\ \qquad \cdot\frac{Z'_{\mathrm{S1}}Z_{\mathrm{S2}}+Z'_{\mathrm{S1}}Z_{\mathrm{S3}}+Z_{\mathrm{S2}}Z_{\mathrm{S3}}}{Z_{\mathrm{S2}}}\frac{1}{-\omega\sqrt{L_{\mathrm{P}}L_{\mathrm{S}}}} \\ m_{22} = -j\omega\sqrt{L_{\mathrm{P}}L_S}\frac{Z_{\mathrm{P1}}+Z_{\mathrm{P2}}}{Z_{\mathrm{P2}}}\frac{1}{Z_{\mathrm{S2}}} \\ n_{22} = \frac{Z_{\mathrm{P1}}Z_{\mathrm{P2}}+Z_{\mathrm{P1}}Z'_{\mathrm{P3}}+Z_{\mathrm{P2}}Z'_{\mathrm{P3}}}{Z_{\mathrm{P2}}} \\ \qquad \cdot\frac{Z'_{\mathrm{S1}}+Z_{\mathrm{S2}}}{Z_{\mathrm{S2}}}\frac{1}{j\omega\sqrt{L_{\mathrm{P}}L_S}}. \end{cases} \tag{18}$$

$$\begin{cases} a_{11} = -j\omega\sqrt{L_{\mathrm{P}}L_{\mathrm{S}}}k\frac{1}{Z_{\mathrm{P2}}}\frac{Z_{\mathrm{S2}}+Z_{\mathrm{S3}}}{Z_{\mathrm{S2}}} + \frac{Z_{\mathrm{P2}}+Z'_{\mathrm{P3}}}{Z_{\mathrm{P2}}}\cdot\frac{Z'_{\mathrm{S1}}Z_{\mathrm{S2}}+Z'_{\mathrm{S1}}Z_{\mathrm{S3}}+Z_{\mathrm{S2}}Z_{\mathrm{S3}}}{Z_{\mathrm{S2}}}\frac{1}{j\omega\sqrt{L_{\mathrm{P}}L_{\mathrm{S}}}k} \\ a_{12} = -j\omega\sqrt{L_{\mathrm{P}}L_{\mathrm{S}}}k\frac{1}{Z_{P2}}\frac{1}{Z_{S2}} + \frac{Z_{\mathrm{P2}}+Z'_{\mathrm{P3}}}{Z_{\mathrm{P2}}}\frac{Z'_{\mathrm{S1}}+Z_{\mathrm{S2}}}{Z_{\mathrm{S2}}}\frac{1}{j\omega\sqrt{L_{\mathrm{P}}L_{\mathrm{S}}}k} \\ a_{21} = -j\omega\sqrt{L_{\mathrm{P}}L_{\mathrm{S}}}k\frac{Z_{\mathrm{P1}}+Z_{\mathrm{P2}}}{Z_{\mathrm{P2}}}\frac{Z_{\mathrm{S2}}+Z_{\mathrm{S3}}}{Z_{\mathrm{S2}}} + \frac{Z_{\mathrm{P1}}Z_{\mathrm{P2}}+Z_{\mathrm{P1}}Z'_{\mathrm{P3}}+Z_{\mathrm{P2}}Z'_{\mathrm{P3}}}{Z_{\mathrm{P2}}}\cdot\frac{Z'_{\mathrm{S1}}Z_{\mathrm{S2}}+Z'_{\mathrm{S1}}Z_{\mathrm{S3}}+Z_{\mathrm{S2}}Z_{\mathrm{S3}}}{Z_{\mathrm{S2}}}\frac{1}{j\omega\sqrt{L_{\mathrm{P}}L_{\mathrm{S}}}k} \\ a_{22} = -j\omega\sqrt{L_{\mathrm{P}}L_{\mathrm{S}}}k\frac{Z_{\mathrm{P1}}+Z_{\mathrm{P2}}}{Z_{\mathrm{P2}}}\frac{1}{Z_{\mathrm{S2}}} + \frac{Z_{\mathrm{P1}}Z_{\mathrm{P2}}+Z_{\mathrm{P1}}Z'_{\mathrm{P3}}+Z_{\mathrm{P2}}Z'_{\mathrm{P3}}}{Z_{\mathrm{P2}}}\cdot\frac{Z'_{\mathrm{S1}}+Z_{\mathrm{S2}}}{Z_{\mathrm{S2}}}\frac{1}{j\omega\sqrt{L_{\mathrm{P}}L_{\mathrm{S}}}k}. \end{cases} \tag{15}$$

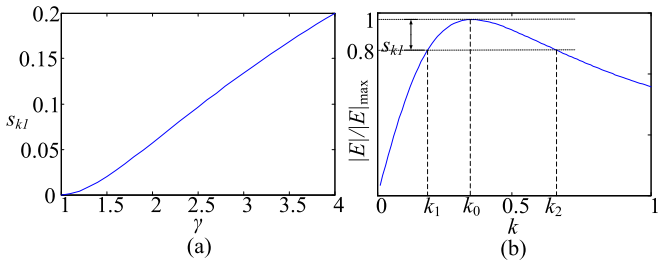

Fig. 3. (a) When $F(R_E) = 1$, s_{k1} varying with γ. (b) When $F(R_E) = 1$, $|E|/|E|_{max}$ varying with k.

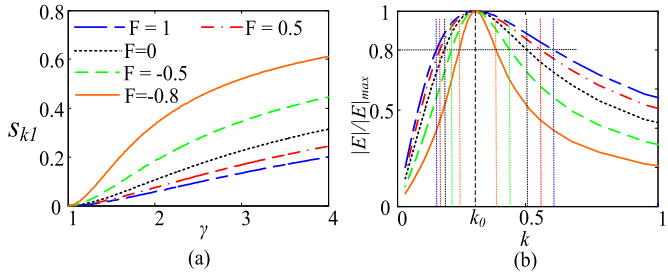

Fig. 4. (a) s_{k1} varying with γ with different values of F. (b) $|E|/|E|_{max}$ varying with k with different values of F.

Substituting (18) into (9), hence

$$\frac{n_{22}}{m_{22}} = -\frac{n_{21}}{m_{21}} = {k_0}^2. \tag{19}$$

For CV mode, to simplify the analysis, the misalignment-tolerant range γ is defined shown as follows:

$$\gamma = \frac{k_2}{k_1} \tag{20}$$

where k_2 and k_1, that are, respectively, the maximum and minimum of the coupling coefficients, are defined to meet the requirements of fluctuation of CV or CC output.

The sensitivity of $|E|$ with respect to k is also defined by (21). $F(R_E)$(defined and analyzed in the appendix) is a function of R_E. $F(R_E)$ increases with increasing R_E. When $R_E = 0$, $R_E = -m_{21}n_{21}/(m_{22}n_{22})$ and R_E is close to ∞, $F = -1$, 0, and 1, respectively. The same F means the same misalignment tolerance. Therefore, the T/T compensation topology that satisfies the formula in (9) can obtain the same misalignment-tolerant capability through design parameters. And, the relationship between s_k, γ, and $F(R_E)$ is obtained in the Appendix

$$s_k = \frac{|E||_{k=k_0} - |E|_{k=k_0+\Delta k}}{|E|_{k=k_0}} = 1 - \sqrt{\frac{2\gamma(1+F(R_E))}{\gamma^2 + 2F(R_E)\gamma + 1}}. \tag{21}$$

When $F(R_E) = 1$ and γ is constant, s_k has a minimum and the misalignment-tolerant capability of the IPT converter is strongest. When $F(R_E) = 1$, (4) can be rewritten as follows:

$$|E| = \frac{R_E}{\left(\sqrt{{R_E}^2{m_{22}}^2 + {m_{21}}^2}\cdot k + \sqrt{{R_E}^2{n_{22}}^2 + {n_{21}}^2}/k\right)}. \tag{22}$$

When $F(R_E) = 1$, s_{k1} varying with γ is shown in Fig. 3(a), and $|E|/|E|_{max}$ varying with k is shown in Fig. 3(b). From Fig. 4(a), s_{k1} increases as γ increases, which means increasing the distance of the misalignment needs to sacrifice fluctuation range of the output voltage. It is more clearly explained in Fig. 3(b). When $F = 1$, 0.5, 0, –0.5, and –0.8, s_{k1} varying with γ is shown in Fig. 4(a), and $|E|/|E|_{max}$ varying with k is shown in Fig. 4(b). For the same misalignment-tolerant range γ, the smaller the F, the bigger the fluctuation of the output voltage. Therefore, the smaller the R_E, the bigger the fluctuation of the output voltage. When $F = 1$, 0.5, 0, –0.5, and –0.8 and $|E|/|E|_{max} > 0.8$ is satisfied, the allowed variation range of the coupling coefficient is 400%, 340%, 276%, 200%, and 160%, respectively. 400% is the limit that can be reached. For CC mode, process of the analysis and result are the same as the CV mode.

Substituting (15) into (9), (23) is obtained, which is the condition of CV output. Substituting (15) into (10), (24) is obtained, which is the condition of CC output.

For CV mode

$$\begin{cases} \frac{Z'_{S1}Z_{S2}+Z'_{S1}Z_{S3}+Z_{S2}Z_{S3}}{Z_{S2}+Z_{S3}} = -(Z'_{S1}+Z_{S2}) \\ \omega^2 L_P L_S {k_0}^2 = \frac{Z_{P1}Z_{P2}+Z_{P1}Z'_{P3}+Z_{P2}Z'_{P3}}{Z_{P1}+Z_{P2}}(Z'_{S1}+Z_{S2}). \end{cases} \tag{23}$$

For CC mode

$$\begin{cases} \frac{Z'_{S1}Z_{S2}+Z'_{S1}Z_{S3}+Z_{S2}Z_{S3}}{Z_{S2}+Z_{S3}} = -(Z'_{S1}+Z_{S2}) \\ \omega^2 L_P L_S {k_0}^2 = -\frac{Z_{P1}Z_{P2}+Z_{P1}Z'_{P3}+Z_{P2}Z'_{P3}}{Z_{P1}+Z_{P2}}(Z'_{S1}+Z_{S2}). \end{cases} \tag{24}$$

IV. Impedance Analysis of S/T Compensation Topologies With High Misalignment Tolerance

Although the compensation topologies such as SPS/SP and PS/SP have misalignment-tolerant capability, the number of compensation components is large. The parameters of the T/S compensation topology cannot satisfy the formula in (9) or (10). Therefore, the T/S compensation topology does not have characteristics independent of coupling and load. However, the parameters of the S/T compensation topology can satisfy formula in (9) or (10). Therefore, the S/T compensation topology has characteristics independent of coupling and load. The S/T compensation topology with simple structure and the same misalignment-tolerant capability is analyzed below and includes S/P, S/SP, S/PS, and S/SPS compensation topologies. Equations (23) and (24) can be rewritten as follows.

For CV mode

$$\begin{cases} \frac{Z'_{S1}Z_{S2}+Z'_{S1}Z_{S3}+Z_{S2}Z_{S3}}{Z_{S2}+Z_{S3}} = -(Z'_{S1}+Z_{S2}) \\ \omega^2 L_P L_S {k_0}^2 = Z'_{P1}(Z'_{S1}+Z_{S2}). \end{cases} \tag{25}$$

For CC mode

$$\begin{cases} \frac{Z'_{S1}Z_{S2}+Z'_{S1}Z_{S3}+Z_{S2}Z_{S3}}{Z_{S2}+Z_{S3}} = -(Z'_{S1}+Z_{S2}) \\ \omega^2 L_P L_S {k_0}^2 = -Z'_{P1}(Z'_{S1}+Z_{S2}) \end{cases} \tag{26}$$

where

$$Z'_{P1} = \frac{1}{j\omega C_1} + j\omega L_P. \tag{27}$$

Z_S is the input impedance angle of the secondary side compensation network A'_s, which can be represented by the following:

$$Z_S = -(Z'_{\mathrm{S1}} + Z_{\mathrm{S2}})\frac{\alpha - 1}{\alpha + 1} \tag{28}$$

where

$$\alpha = \frac{Z_{\mathrm{S2}} + Z_{\mathrm{S3}}}{R_{\mathrm{E}}}. \tag{29}$$

According to (25) and (26), the system input impedance angles of the CC and CV modes can be represented by the following equations.

For CV mode

$$Z_{\mathrm{in}} = \frac{{Z_{\mathrm{M}}}^2}{Z_{\mathrm{S1}} + Z_{\mathrm{S2}}}\frac{\alpha + 1}{\alpha - 1} - \frac{{Z_{M0}}^2}{Z_{\mathrm{S1}} + Z_{\mathrm{S2}}} \tag{30}$$

For CC mode

$$Z_{\mathrm{in}} = \frac{{Z_{\mathrm{M}}}^2}{Z_{\mathrm{S1}} + Z_{\mathrm{S2}}}\frac{\alpha + 1}{\alpha - 1} + \frac{{Z_{\mathrm{M0}}}^2}{Z_{\mathrm{S1}} + Z_{\mathrm{S2}}}. \tag{31}$$

In order to simplify the analysis, (28), (30), and (31) are transformed as follows:

$$Z'_{\mathrm{S}} = -\frac{Z'_{\mathrm{S1}} + Z_{\mathrm{S2}}}{|Z'_{\mathrm{S1}} + Z_{\mathrm{S2}}|}\frac{\alpha - 1}{\alpha + 1} = 1\angle\theta_{\mathrm{S}}. \tag{32}$$

For CV mode

$$Z'_{\mathrm{in}} = \mathrm{j}K_{\mathrm{MS}}\frac{\alpha + 1}{\alpha - 1} - \mathrm{j}K_{\mathrm{MS0}} \tag{33}$$

For CC mode

$$Z'_{\mathrm{in}} = \mathrm{j}K_{\mathrm{MS}}\frac{\alpha + 1}{\alpha - 1} + \mathrm{j}K_{MS0} \tag{34}$$

where

$$\begin{cases} K_{\mathrm{MS}} = \frac{{Z_{\mathrm{M}}}^2|Z_{\mathrm{S1}}+Z_{\mathrm{S2}}|}{j(Z_{\mathrm{S1}}+Z_{\mathrm{S2}})\left|{Z_{\mathrm{M0}}}^2\right|} = \pm\frac{k^2}{{k_0}^2} \\ K_{\mathrm{MS0}} = \frac{{Z_{\mathrm{M0}}}^2|Z_{\mathrm{S1}}+Z_{\mathrm{S2}}|}{j(Z_{\mathrm{S1}}+Z_{\mathrm{S2}})\left|{Z_{\mathrm{M0}}}^2\right|} = \pm 1. \end{cases} \tag{35}$$

From (33) and (34), the input impedance angle of the system may be capacitive, and the ZVS of the inverter cannot be realized. In order to implement ZVS in the load range, where the system has strong misalignment-tolerant capability, it is necessary to satisfy the condition $Z'_{\mathrm{P1}}/\mathrm{j} > 0$. Therefore, θ_{S} and θ_{in} can be calculated as (36) and (37), where θ_{in} is the primary input impedance angle.

For CV mode

$$\begin{cases} \theta_{\mathrm{S}} = \arctan\frac{|\alpha|^2-1}{2|\alpha|}(-90^{\mathrm{o}} < \theta_{\mathrm{S}} < 90^{o}) \\ Z'_{\mathrm{in}} = \frac{k^2}{{k_0}^2}\angle - \theta_{\mathrm{S}} + 1\angle 90^{o} \\ \theta_{\mathrm{in}} = \arctan\frac{{k_0}^2-k^2\sin(\theta_{\mathrm{S}})}{k^2\cos(\theta_{\mathrm{S}})}. \end{cases} \tag{36}$$

For CC mode

$$\begin{cases} \theta_{\mathrm{S}} = \arctan\frac{1-|\alpha|^2}{2|\alpha|}(-90^{\mathrm{o}} < \theta_{\mathrm{S}} < 90^{o}) \\ Z'_{\mathrm{in}} = \frac{k^2}{{k_0}^2}\angle - \theta_{\mathrm{S}} + 1\angle 90^{o} \\ \theta_{\mathrm{in}} = \arctan\frac{{k_0}^2-k^2\sin(\theta_{\mathrm{S}})}{k^2\cos(\theta_{\mathrm{S}})}. \end{cases} \tag{37}$$

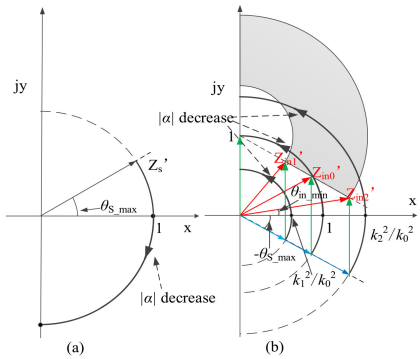

Fig. 5. (a) Relationship among Z'_S, θ_S, and α in CV mode. (b) Relationship among Z'_{in}, α, θ_{in}, and k in CV mode.

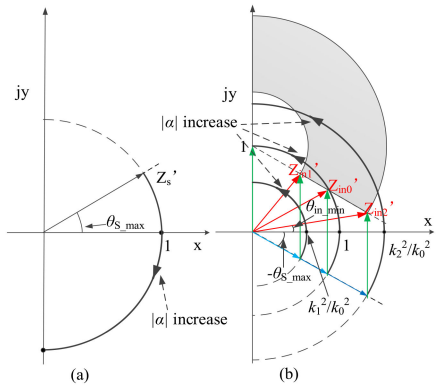

Fig. 6. (a) Relationship among Z'_S, θ_S, and α in CC mode. (b) Relationship among Z'_{in}, α, θ_{in}, and k in CC mode.

For CV mode, the relationship among Z_{S}', θ_{S}, and α obtained by (32) and (36) can be presented in Fig. 5(a), and the relationship among Z'_{in}, α, θ_{in}, and k can be presented in Fig. 5(b), where k_1 and k_2 are the minimum and maximum values of the coupling coefficient, respectively. $Z_{\mathrm{in1}}{}'$, $Z'_{\mathrm{in}\,0}$, and $Z'_{\mathrm{in}\,2}$ are the input impedances when coupling coefficients is equal to k_1, $k_{0,}$ and k_2, respectively. $\theta_{\mathrm{S}\cdot\mathrm{max}}$ is the maximum value of θ_{S} at rated load. $\theta_{\mathrm{in}\cdot\mathrm{min}}$ is the minimum value of θ_{in} at rated load. θ_{S} decreases as α decreases. When the coupling coefficient is constant, θ_{in} increases as α decreases. When the load resistance is constant, θ_{in} decreases as k increases. The gray fan-shaped ring is the working area of Z'_{in}.

For CC mode, the relationship among Z'_S, θ_S, and α obtained by (32) and (37) can be presented in Fig. 6(a), and the relationship among Z'_{in}, α, θ_{in}, and k can be presented in Fig. 6(b). θ_{S} decreases as α increases. When the coupling coefficient is constant, θ_{in} increases as α increases. When the load resistance is constant, θ_{in} decreases as k increases. θ_{S} have the maximum value $\theta_{\mathrm{S\_max}}$ at rated load. θ_{in} have the minimum value $\theta_{\mathrm{in\_min}}$ at rated load.

The application of this article is that the self-inductance of LCT does not change with the coupling coefficient or the change is small. For example, an LCT without ferrite or an LCT with a relatively big ratio of the transmission distance and the biggest

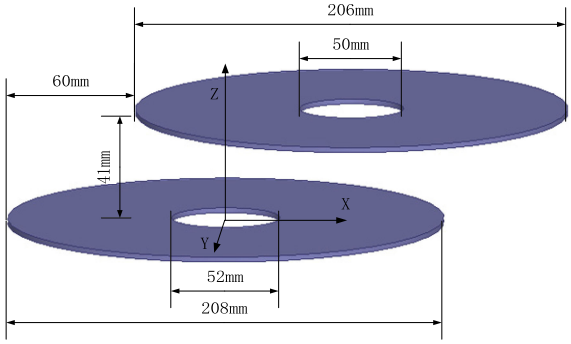

Fig. 7. Schematic diagram of LCT misalignment.

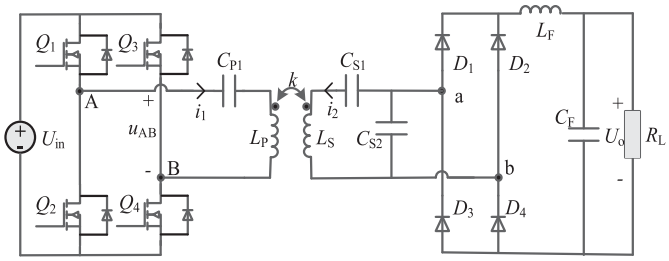

Fig. 8. Schematic of S/SP compensated IPT system with CV mode.

size of LCT are used in the application. Therefore, efficiency of the LCT can be expressed as follows:

$$\eta_t = (1 - \frac{|I_{\rm in}|^2 R_1 + |I_S|^2 R_2}{|I_{\rm in}|^2 |Z_{\rm in}| \cos\theta_{\rm in}}) \times 100\% = (1 - \frac{R_1 + (k^2 |Z'_{\rm P1}| R_2)/(k_0{}^2 |Z'_{\rm S1} + Z_{\rm S2}|)}{|Z_{\rm in}| \cos\theta_{\rm in}}) \times 100\%. \quad (38)$$

From (38), it can be seen that the transformer transmission efficiency increases when the real number of the input impedance increases. With the same coupling coefficient, the transmission efficiency of LCT is the highest when $|\alpha| = 1$. When $|\alpha| = 1$, the $\theta_{\rm in}$ of the CV mode or CC mode is as follows:

$$\theta_{\rm in}\,|_{|\alpha|=1} = \arctan\frac{k_1}{k_2}. \quad (39)$$

V. Experimental Results

Because the misalignment tolerance of the compensation topology designed in this article is not limited by LCT, the most commonly used circular coil is adopted. The schematic diagram of LCT misalignment is shown in Fig. 7. The range of the misaligned distance is 0–60 mm. In order to demonstrate the applicability of the proposed topology and the above analysis, two experimental prototype of the IPT system with S/SP compensation topology system was designed and built. They have the output characteristics of CV and CC, respectively. And the planar circular coil without ferrites is used in the prototypes. The circuit diagram of the S/SP compensation topology system is shown in Fig. 8. The compensation capacitor C_{s2} causes that the input voltage of the rectifier cannot be changed immediately, but the input current can be changed immediately. Therefore, *LC* filtering is required after the rectifier.

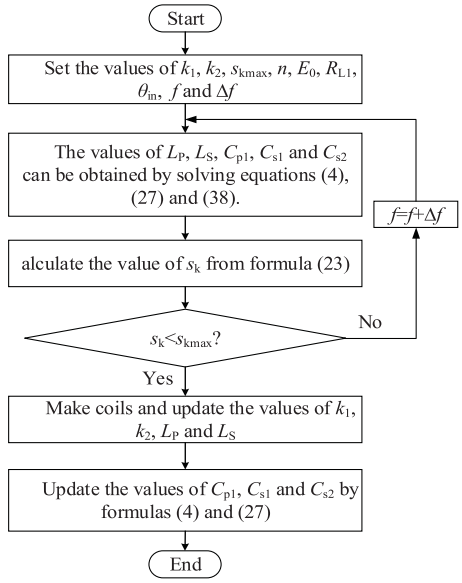

Fig. 9. Flowchart of design parameters.

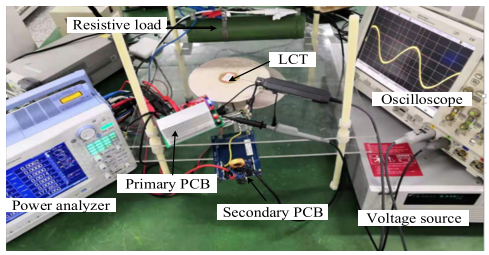

Fig. 10. Photograph of the experimental setup with CV mode.

TABLE I
Parameters of S/SP Compensation Topology With CV Mode

Circuit component	Type and value
Frequency	200 kHz
Coupling coefficient	$k_{\rm min}$ =0.211 k_0 = 0.283 $k_{\rm max}$ = 0.355
Self-inductance of LCT	L_P = 60.8 μH L_S = 63.3 μH
Compensation capacitance	C_{p1} = 13.31 nF C_{s1} = 15.57 nF C_{s2} = 13.92 nF
Load resistance R_L	R_1 = 36 Ω R_2 = 72 Ω R_3 = 108 Ω

Flowchart of design parameters is shown in Fig. 9, where $s_{\rm kmax}$ is the maximum voltage fluctuation ratio, n is the primary and secondary side turns ratio, E_0 is the voltage ratio when $k = k_0$, $R_{\rm L1}$ is the resistance of the rated load, and Δf is the step value of changing the frequency.

Fig. 10 is the photograph of the experimental setup. Design S/SP compensation topology by above analysis. The main parameters of the system are shown in Table I. $u_{\rm AB}$ is the output voltage of the inverter and $U_{\rm o}$ is the voltage of the load. The output voltage $U_{\rm o}$ varying with the coupling coefficient and load are as shown in Fig. 11. When the coupling coefficient is equal to k_0, the output voltage has a maximum value under different loads. It is consistent with the previous analysis. However, as resistance

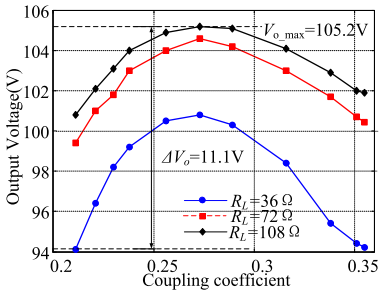

Fig. 11. S/SP compensation topology with CV mode varying with the coupling coefficient and load.

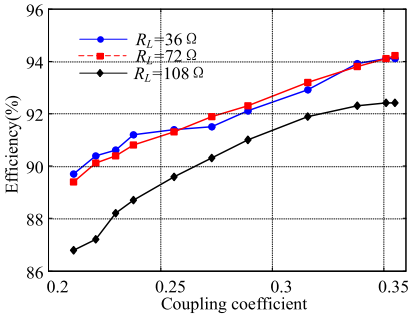

Fig. 12. Efficiency varying with the coupling coefficient and load.

of the load increases, the maximum value of the output voltage will increase slightly. It is caused by the parasitic resistance of the circuit and tiny error in each of the compensation parameters.

In order to indicate the ability of the system to stabilize the voltage, the output voltage fluctuation range g_{R_CV} is defined by (40), where $U_{\text{out-max}}$ and $U_{\text{out-min}}$ are the maximum and minimum output voltages of IPT system within a predetermined coupling coefficient range. The output voltage fluctuation range is 5.57%. The system has strong misalignment-tolerant capability. In addition, the fluctuation of the output voltage with varying coupling coefficient decreases with the increase of the load resistance. This is consistent with the theoretical analysis.

$$g_{R\_CV} = (U_{\text{out-max}} - U_{\text{out-min}})/(U_{\text{out-max}} + U_{\text{out-min}}). \tag{40}$$

The efficiency of the system was measured using a power analyzer PX8000. Fig. 12 shows the efficiency of the system with CV mode varying with the coupling coefficient under different loads. The system efficiency decreases as k decreases. And the system efficiency is basically the same when $R_L = 36\ \Omega$ and $R_L = 72\ \Omega$. Fig. 13 shows the efficiency of the S/SP compensation topology with CV mode varying with the resistive load for $k = k_{\max}$. It can be seen that the system efficiency is not the maximum at rated load, and the efficiency increases first and then decreases as the load resistance increases. The reason is that the loss of the loosely coupled transformer and the loss of the compensation component in series with it and the conduction loss of the MOSFET account for a large proportion of the system loss, so the trend of system efficiency with load changes is greatly affected by them. This is consistent with the trend of efficiency varying with load reflected by (38).

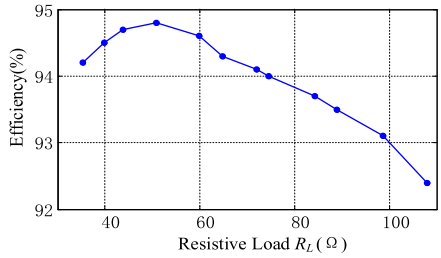

Fig. 13. Efficiency of the S/SP compensation topology with CV mode varying with the resistive load for $k = k_{\max}$.

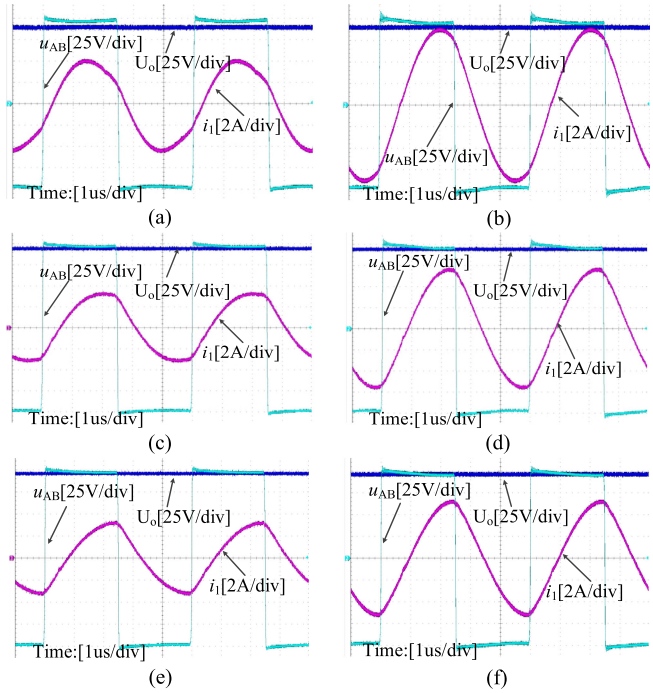

Fig. 14. Waveforms of the S/SP compensation topology with CV mode for various load under maximum and minimum coupling coefficient. (a) $R_L = R_1$, $k = k_{\max}$. (b) $R_L = R_1$, $k = k_{\min}$. (c) $R_L = R_2$, $k = k_{\max}$. (d) $R_L = R_2$, $k = k_{\min}$. (e) $R_L = R_3$, $k = k_{\max}$. (f) $R_L = R_3$, $k = k_{\min}$.

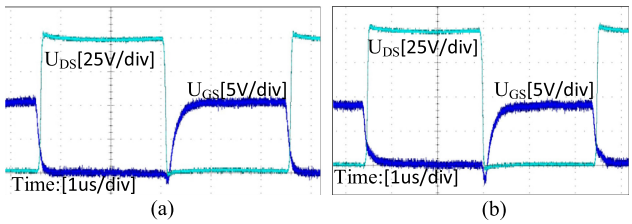

Fig. 15. Voltage waveform of system with the CV mode between gate-source voltage U_{GS} and drain-source voltage U_{DS}. (a) Inverter lower MOSFET. (b) Inverter upper MOSFET.

Fig. 14 is the waveforms of the S/SP compensation topology with CV mode for various load under maximum and minimum coupling coefficient. Their θ_{in} is greater than zero.

θ_{in} increases as R_L increases, and θ_{in} increases as k decreases. It is consistent with the previous analysis. Fig.15 shows the wave of the voltage between gate and source U_{GS} and voltage between drain and source U_{DS}. They all implemented ZVS.

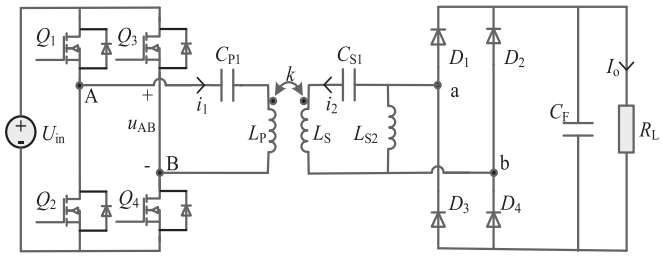

Fig. 16. Schematic of S/SP compensated IPT system with CC mode.

TABLE II
PARAMETERS OF S/SP COMPENSATION TOPOLOGY WITH CC MODE

Circuit component	Type and value		
Frequency	200 kHz		
Coupling coefficient	k_{min} =0.211	k_0 = 0.283	k_{max} = 0.355
Self-inductance of LCT	L_P = 60.8 μH	L_S = 63.3 μH	
Compensation components	C_{p1} = 13.31 nF	C_{s1} = 7.35 nF	
	L_{s2} = 45.6 uH		
Load resistance R_L	R_1 = 36 Ω	R_2 = 72 Ω	R_3 = 108 Ω

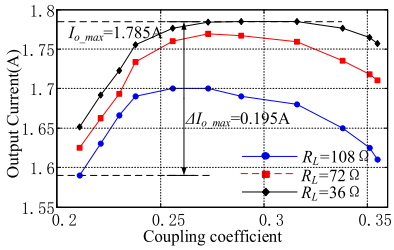

Fig. 17. S/SP compensation topology with CC mode varying with the coupling coefficient and load.

The circuit diagram of the S/SP compensation topology with CC mode is shown in Fig. 16. Compared with Fig. 8, L_{s2} replaces C_{s2}, which causes the input current of the rectifier to not change immediately, but the input voltage can. Therefore, C filtering is required after the rectifier. The secondary parallel component of the S/SP compensation topology with CC output is the inductor. This is different from the CV mode. I_o is the laod current. The flowchart of design parameters in CC mode is shown in Fig. 9, and the main parameters of the system are shown in Table II. Fig. 17 is the current of S/SP compensation topology with CC mode varying with the coupling coefficient and load. Same as CV mode, the output current fluctuation range g_{R_CC} is defined by (41), here $I_{\text{out-max}}$ and $I_{\text{out-min}}$ are the maximum and minimum output currents of the IPT system. The output current fluctuation range is 5.78%. The system also has strong misalignment-tolerant capability

$$g_{R\_CC} = (I_{\text{out-max}} - I_{\text{out-min}})/(I_{\text{out-max}} + I_{\text{out-min}}). \tag{41}$$

Fig. 18 shows the efficiency of the system with CC mode varying with the coupling coefficient and load. Efficiency at half load is higher than efficiency at rated. And, Fig. 19 shows the efficiency varying with the resistive load for $k = k_{\max}$.

It can be seen that the system efficiency is not the maximum at rated load, and the efficiency increases first and then decreases

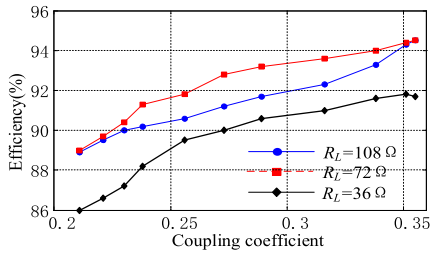

Fig. 18. Efficiency of the system with CC mode varying with the coupling coefficient and load.

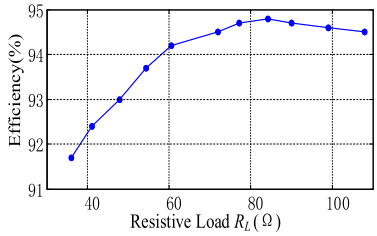

Fig. 19. Efficiency of the S/SP compensation topology with CC mode varying with the resistive load for $k = k_{\max}$.

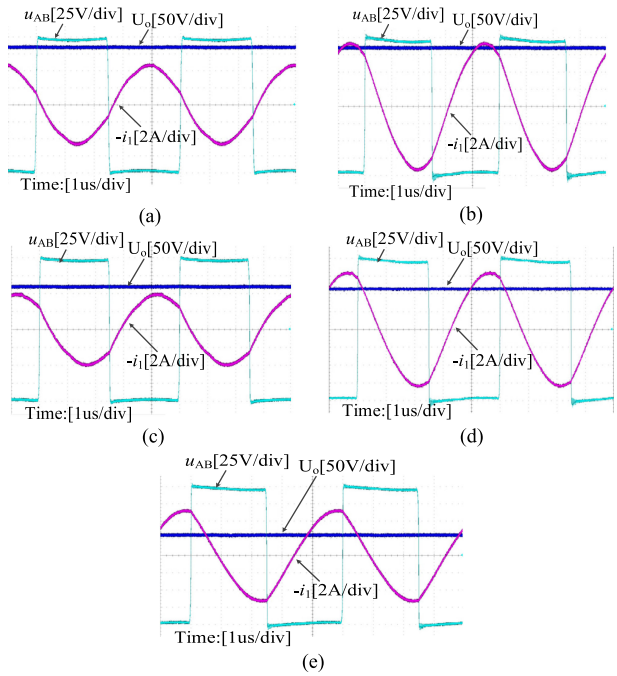

Fig. 20. Waveforms of the S/SP compensation topology with CC mode for various load under maximum and minimum coupling coefficient. (a) $R_L = R_3$, $k = k_{\max}$. (b) $R_L = R_3$, $k = k_{\min}$. (c) $R_L = R_2$, $k = k_{\max}$. (d) $R_L = R_2$, $k = k_{\min}$. (e) $R_L = R_1$, $k = k_{\min}$.

as the load resistance increases. The reason is the same as the CV mode. The highest efficiency is 94.8 and the lowest is 86%. The designed system is characterized by high efficiency and strong misalignment tolerance.

Fig. 20 is the waveforms of the S/SP compensation topology with CC mode for various load under maximum and minimum coupling coefficient. The waveform of the current is the reverse value of the output current. θ_{in} increases as R_L decreases and

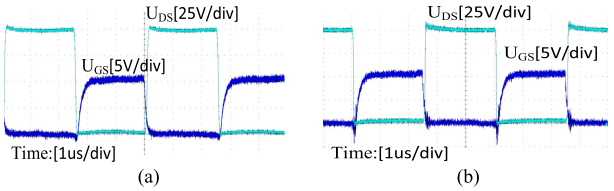

Fig. 21. Voltage waveform of system with the CC mode between gate–source voltage U_{GS} and drain–source voltage U_{DS}. (a) Inverter lower MOSFET. (b) Inverter upper MOSFET.

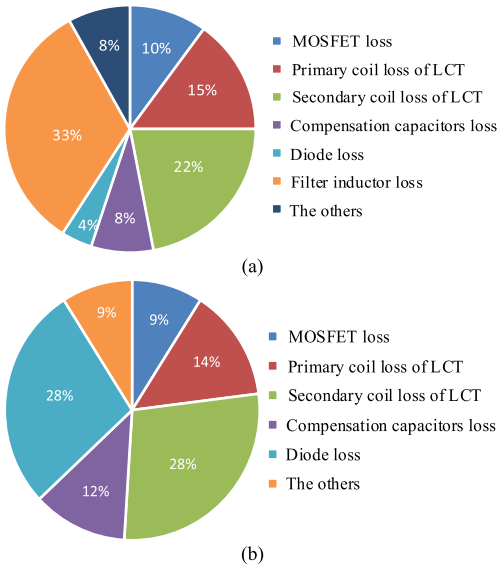

Fig. 22. When the efficiency of the S/SP compensation topology is highest, the loss distribution of each part. (a) CV mode. (b) CC mode.

θ_{in} increases as k decreases. The similarity between CV mode and CC mode is that θ_{in} increases with the decrease of output power caused by the change of load and θ_{in} increases with the decrease of k. It is consistent with the previous analysis. Fig. 21 is the voltage waveform of system with the CC mode between gate–source voltage U_{GS} and drain–source voltage U_{DS}. They all implemented ZVS.

The losses of the S/SP compensation topology at the highest efficiency in CV mode and CC mode are analyzed separately. The loss distribution of each part is shown in Fig. 22. The main losses are: MOSFET loss, primary coil loss of LCT, secondary coil loss of LCT, compensation capacitors loss, diode loss, filter inductor loss, and others.

VI. Conclusion

Based on the analysis of the two-port network of the IPT system, the conditions that the output voltage/current is insensitive to the coupling coefficient and the load resistance are found. The compensation topologies with secondary parallel compensation component have a strong capability of misalignment tolerance if the parameters of the compensation circuit are properly designed, such as S/P, S/SP, S/PS, S/SPS, PS/SP, SPS/SP and SPS/SPS compensation topologies. Moreover, the number of compensation components used in the S/T (S/P, S/SP, S/PS and S/SPS) compensation topology is small and the structure is simple. Therefore, its impedance characteristics are analyzed in this article to help achieve ZVS. The transformer efficiency transfer formula is given. Finally, build two IPT systems with CV and CC modes, respectively. Their output voltage or current fluctuation range is 5.57% and 5.78%, respectively. The highest efficiency of systems with CV and CC modes is 94.7% and 94.8%, respectively. The minimum efficiency of systems with CV and CC modes is 86.8% and 86.0%, respectively. The designed system has advantages like high efficiency and strong misalignment tolerance.

Appendix

For CV mode, substituting (17) into (4), $|E|^2$ can be calculated as (A1)

$$|E|^2 = \frac{{R_{\mathrm{E}}}^2}{({R_{\mathrm{E}}}^2{m_{22}}^2 + {m_{21}}^2)} \cdot \frac{1}{f(K)} \tag{A1}$$

$$f(K) = K + \frac{{R_{\mathrm{E}}}^2{n_{22}}^2 + {n_{21}}^2}{({R_{\mathrm{E}}}^2{m_{22}}^2 + {m_{21}}^2)K} + \frac{2{R_{\mathrm{E}}}^2 m_{22}n_{22} + 2m_{21}n_{21}}{({R_{\mathrm{E}}}^2{m_{22}}^2 + {m_{21}}^2)} \tag{A2}$$

where $K = k^2$ and ${R_{\mathrm{E}}}^2{m_{22}}^2 + {m_{21}}^2 \neq 0$. The derivative of $f(K)$ with respect to k can be calculated by (A3). From (19), when $K = K_0 = {k_0}^2$, $\delta f(K)/\delta K < 0$. When $K < K_0$, $\delta f(K)/\delta K < 0$. And, when $K > K_0$, $\delta f(K)/\delta K > 0$. Therefore, $f(K)$ has the minimum value $f(K_0)$. Substituting K_0 into (A2), (A2) can be calculated as (A4). Since $-1 \leq F \leq 1$, $f(K) \geq f(K_0) \geq 0$. The derivative of F with respect to ${R_E}^2$ can be calculated by (A6). From (19), $\delta F/\delta {R_{\mathrm{E}}}^2 > 0$. F increases with increasing R_{E}. When $R_{\mathrm{E}} = 0$, $R_{\mathrm{E}} = -m_{21}n_{21}/(m_{22}n_{22})$, and R_{E} is close to ∞, $F = -1$, 0, and 1, respectively. To facilitate the analysis, when $K = K_0$, the sensitivity of $1/|E|^2$ with respect to K is defined by (A7), where $\varepsilon_K = (\Delta K + K_0)/K_0$. Then when $k = k_0$, the sensitivity of $|E|$ with respect to k is also defined by (A8), where $K_0 + \Delta K = (k_0 + \Delta k)^2$. The smaller the S_K and s_k, the smaller the sensitivity. For the same $\Delta K/K_0$, the bigger the F, the smaller the S_K and s_k. Therefore, for the same $\Delta k/k$, the bigger the F, the smaller the sensitivity of $|E|$ with respect to k, it means the misalignment-tolerant capability will be stronger. And, the coupling-independent CV or CC output will be more constant

$$\frac{\delta f(K)}{\delta K} = 1 - \frac{{R_E}^2{n_{22}}^2 + {n_{21}}^2}{({R_E}^2{m_{22}}^2 + {m_{21}}^2)K^2} \tag{A3}$$

$$f(K_0) = 2\sqrt{\frac{{R_E}^2{n_{22}}^2 + {n_{21}}^2}{({R_E}^2{m_{22}}^2 + {m_{21}}^2)}} + \frac{2{R_E}^2 m_{22}n_{22} + 2m_{21}n_{21}}{({R_E}^2{m_{22}}^2 + {m_{21}}^2)} = 2\sqrt{\frac{{R_E}^2{n_{22}}^2 + {n_{21}}^2}{({R_E}^2{m_{22}}^2 + {m_{21}}^2)}}(1 + F) \tag{A4}$$

$$-1 \leq F = \frac{{R_E}^2 m_{22}n_{22} + m_{21}n_{21}}{\sqrt{({R_E}^2{m_{22}}^2 + {m_{21}}^2)({R_E}^2{n_{22}}^2 + {n_{21}}^2)}} \leq 1 \tag{A5}$$

$$\frac{\delta F}{\delta {R_E}^2} = \frac{1}{2}\frac{({R_E}^2 m_{22}n_{22} - m_{21}n_{21})(m_{22}n_{21} - m_{21}n_{22})^2}{\left[({R_E}^2 {m_{22}}^2 + {m_{21}}^2)({R_E}^2 {n_{22}}^2 + {n_{21}}^2)\right]^{\frac{3}{2}}} > 0 \tag{A6}$$

$$S_K = \frac{f(K_0 + \Delta K) - f(K_0)}{f(K_0)} = \frac{\frac{1}{\varepsilon_K} + \varepsilon_K - 2}{2 + 2F} \tag{A7}$$

$$s_k = \frac{|E||_{k=k_0} - |E|_{k=k_0+\Delta k}}{|E|_{k=k_0}} = 1 - \sqrt{\frac{1}{S_K + 1}}. \tag{A8}$$

From (A7) and (A8), the strongest misalignment-tolerant capability of IPT converter without feedback control, compensation and parasitic parameter changes and the hybrid compensation is found. There are two solutions of ε_K about the formula in (A7), as shown in (A9) and (A10), where $\varepsilon_{K2} \times \varepsilon_{K1} = 1$, $K_2 = \varepsilon_{K2} K_0$, $K_1 = \varepsilon_{K1} K_0$, $k_2 = \sqrt{\varepsilon_{K2}} k_0$, and $k_1 = \sqrt{\varepsilon_{K1}} k_0$. k_2 and k_1, that are, respectively, the maximum and minimum of the coupling coefficients, are defined to meet the requirements of fluctuation of CV or CC output

$$\varepsilon_{K2} = 1 + (1+F)\left(\frac{1}{(1-s_k)^2} - 1\right) + \sqrt{\left(1 + (1+F)\left(\frac{1}{(1-s_k)^2} - 1\right)\right)^2 - 1} \tag{A9}$$

$$\varepsilon_{K1} = 1 + (1+F)\left(\frac{1}{(1-s_k)^2} - 1\right) - \sqrt{\left(1 + (1+F)\left(\frac{1}{(1-s_k)^2} - 1\right)\right)^2 - 1}. \tag{A10}$$

To simplify the analysis, the misalignment-tolerant range γ is defined as follows:

$$\gamma = \frac{k_2}{k_1} = \sqrt{\frac{\varepsilon_{K2}}{\varepsilon_{K1}}}. \tag{A11}$$

REFERENCES

[1] Z. Zhang, H. Pang, A. Georgiadis, and C. Cecati, "Wireless power transfer - an overview," *IEEE Trans. Ind. Electron.*, vol. 66, no. 2, pp. 1044–1058, Feb. 2019.

[2] Z. Zhang and K. T. Chau, "Homogeneous wireless power transfer for move-and-charge," *IEEE Trans. Power Electron.*, vol. 30, no. 11, pp. 6213–6220, Nov. 2015.

[3] C.-S. Wang, O. H. Stielau, and G. A. Covic, "Design considerations for a contactless electric vehicle battery charger," *IEEE Trans. Ind. Electron.*, vol. 52, no. 5, pp. 1308–1314, Oct. 2005.

[4] S. Jung, H. Lee, C. S. Song, J.-H. Han, W.-K. Han, and G. Jang, "Optimal operation plan of the online electric vehicle system through establishment of a DC distribution system," *IEEE Trans. Power Electron.*, vol. 28, no. 12, pp. 5878–5889, Dec. 2013.

[5] J. P. C. Smeets, T. T. Overboom, J. W. Jansen, and E. A. Lomonova, "Comparison of position-independent contactless energy transfer systems," *IEEE Trans. Power Electron.*, vol. 28, no. 4, pp. 2059–2067, Apr. 2013.

[6] Y. Liao, S. Zhang, G. Xu, and M. Xing, "A novel imaging algorithm for circular scanning SAR based on the Cardano's formula," in *Proc. IET Int. Radar Conf.*, 2013, pp. 1–5.

[7] S. Wang, J. Chen, Z. Hu, C. Rong, and M. Liu, "Optimisation design for series–series dynamic WPT system maintaining stable transfer power," *IET Power Electron.*, vol. 10, no. 9, pp. 987–995, 2017.

[8] J. L. Villa, J. Sallan, J. F. Sanz Osorio, and A. Llombart, "High-Misalignment tolerant compensation topology for ICPT systems," *IEEE Trans. Ind. Electron.*, vol. 59, no. 2, pp. 945–951, Feb. 2012.

[9] J. Zhao, T. Cai, S. Duan, H. Feng, C. Chen, and X. Zhang, "A general design method of primary compensation network for dynamic WPT system maintaining stable transmission power," *IEEE Trans. Power Electron.*, vol. 31, no. 12, pp. 8343–8358, Dec. 2016.

[10] Y. Yao, Y. Wang, X. Liu, X. Lu, and D. G. Xu, "Analysis and design of an S/SP compensated IPT system to minimize output voltage fluctuation versus coupling coefficient and load variation," *IEEE Trans. Veh. Technol.*, vol. 67, no. 10, pp. 9262–9272. Oct. 2018.

[11] H. Feng, T. Cai, S. Duan, J. Zhao, X. Zhang, and C. Chen, "An LCC-Compensated resonant converter optimized for robust reaction to large coupling variation in dynamic wireless power transfer," *IEEE Trans. Ind. Electron.*, vol. 63, no. 10, pp. 6591–6601, Oct. 2016.

[12] Y. Wang, Y. Yao, X. Liu, D. Xu, and L. Cai, "An LC/S compensation topology and coil design technique for wireless power transfer," *IEEE Trans. Power Electron.*, vol. 33, no. 3, pp. 2007–2025, Mar. 2018.

[13] S. Li, W. Li, J. Deng, T. D. Nguyen, and C. C. Mi, "A double-sided LCC compensation network and its tuning method for wireless power transfer," *IEEE Trans. Veh. Technol.*, vol. 64, no. 6, pp. 2261–2273, Jun. 2015.

[14] W. Li, H. Zhao, S. Li, J. Deng, T. Kan, and C. C. Mi, "Integrated LCC compensation topology for wireless charger in electric and plugin electric vehicles," *IEEE Trans. Ind. Electron.*, vol. 62, no. 7, pp. 4215–4225, Jul. 2015.

[15] J. Hou, Q. Chen, S. Wong, C. K. Tse, and X. Ruan, "Analysis and control of series/series-parallel compensated resonant converter for contactless power transfer," *IEEE J. Emer. Sel. Top ics Power Electron.*, vol. 3, no. 1, pp. 124–136, Mar. 2015.

[16] J. Hou, Q. Chen, X. Ren, S. C. Wong, and C. K. Tse, "Steady-state analysis of series/series-parallel compensated contactless resonant converter," in *Proc. IEEE 79th Veh. Technol. Conf.*, 2014, pp. 1–5.

[17] J. Hou, Q. Chen, X. Ren, X. Ruan, S. C. Wong, and C. K. Tse, "Precise characteristics analysis of series/series-parallel compensated contactless resonant converter," *IEEE J. Emerg. Sel. Topics Power Electron.*, vol. 3, no. 1, pp. 101–110, Mar. 2015.

[18] Y. Wang, J. Mai, Y. Yao, and D. Xu, "Analysis and design of an IPT system based on S/SP compensation with improved output voltage regulation," *IEEE Trans. Ind. Informat.*, vol. 16, no. 5, pp. 3256–3266, May 2020.

[19] X. Qu, Y. Jing, H. Han, S. C. Wong, and C. K. Tse, "Higher order compensation for inductive-power-transfer converters with constant-voltage or constant-current output combating transformer parameter constraints," *IEEE Trans. Power Electron.*, vol. 32, no. 1, pp. 394–405, Jan. 2017.

[20] X. Qu, H. Han, S. C. Wong, C. K. Tse, and W. Chen, "Hybrid IPT topologies with constant current or constant voltage output for battery charging applications," *IEEE Trans. Power Electron.*, vol. 30, no. 11, pp. 6329–6337, Nov. 2015.

[21] C. Auvigne, P. Germano, D. Ladas, and Y. Perriard, "A dual-topology ICPT applied to an electric vehicle battery charger," in *Proc. Int. Conf. Electron. Mach.*, Mar. 2012, pp. 2287–2292.

[22] R. Mai, Y. Chen, Y. Li, Y. Zhang, G. Cao, and Z. He, "Inductive power transfer for massive electric bicycles charging based on hybrid topology switching with a single inverter," *IEEE Trans. Power Electron.*, vol. 32, no. 8, pp. 5897–5906, Aug. 2017.

[23] J. Hou, Q. Chen, Z., Zhang, S. C. Wong, and C. K. Tse, "Analysis of output current characteristics for higher order primary compensation in inductive power transfer systems," *IEEE Trans. Power Electron.*, vol. 33, no. 8, pp. 6807–6821, Aug. 2017.

[24] Y. Wang, Y. Yao, X. Liu, and D. Xu, "S/CLC compensation topology analysis and circular coil design for wireless power transfer," *IEEE Trans. Transp. Electrific.*, vol. 3, no. 2, pp. 496–507, Jun. 2017.

[25] Y. Chen, B. Yang, Z. Kou, Z. He, G. Cao, and R. Mai, "Hybrid and reconfigurable IPT systems with high-misalignment tolerance for constant-current and constant-voltage battery charging," *IEEE Trans. Power Electron.*, vol. 33, no. 10, pp. 8259–8269, Oct. 2018.

[26] L. Zhao, D. J. Thrimawithana, and U. K. Madawala, "Hybrid bidirectional wireless EV charging system tolerant to pad misalignment," *IEEE Trans. Ind. Electron.*, vol. 64, no. 9, pp. 7079–7086, Sep. 2017.

[27] Y. Chen *et al.*, "A hybrid inductive power transfer system with misalignment tolerance using quadruple-D quadrature pads," *IEEE Trans. Power Electron.*, vol. 35, no. 6, pp. 6039–6049, Jun. 2020.

Jianwei Mai (Student Member, IEEE) was born in Henan, China, in 1994. He received the B.S. degree in electrical engineering in 2017 from the Harbin Institute of Technology, Harbin, China, where he is currently working toward the Ph.D. degree.

His research interests include inductive power transfer and magnetic coupling structure design.

Yijie Wang (Senior Member, IEEE) was born in Heilongjiang, China, in 1982. He received the B.S., M.S., and Ph.D. degrees in electrical engineering from the Harbin Institute of Technology, Harbin, China, in 2005, 2007, and 2012, respectively.

From 2012 to 2014, he was a Lecturer with the Department of Electrical and Electronics Engineering, Harbin Institute of Technology. Since 2015, he has been an Associate Professor with the Department of Electrical and Electronics Engineering, Harbin Institute of Technology. His research interests include dc–dc converters, soft-switching power converters, power factor correction circuits, digital control electronic ballasts, and LED lighting systems.

Dr. Wang is an Associate Editor of the IEEE TRANSACTIONS ON INDUSTRIAL ELECTRONICS, IEEE JOURNAL OF EMERGING AND SELECTED TOPICS IN POWER ELECTRONICS, IEEE ACCESS, *IET Power Electronics,* and *Journal of Power Electronics*.

Yousu Yao (Member, IEEE) was born in Jiangsu, China, in 1991. He received the B.S. and Ph.D. degrees in electrical engineering from the Harbin Institute of Technology, Harbin, China, in 2014 and 2019, respectively.

He is currently an Associate Professor with the School of Electrical Engineering and Automation, Harbin Institute of Technology. He has authored or coauthored more than 30 journal and conference papers and holds seven patents. His current research interests include wireless power transfer, dc–dc converter, magnetic coupler design, and simultaneous wireless power and data transfer.

Dr. Yao was the recipient of the First Prize Paper Award from the IEEE TRANSACTIONS ON POWER ELECTRONICS, and the Best Paper Awards from ICEMS 2019, SPEED 2019, and ITEC Asia-Pacific 2017.

Dianguo Xu (Fellow, IEEE) was born in Heilongjiang, China, in 1960. He received the B.S. degree in control engineering from Harbin Engineering University, Harbin, China, in 1982, and the M.S. and Ph.D. degrees in electrical engineering from the Harbin Institute of Technology (HIT), Harbin, China, in 1984 and 1989, respectively.

In 1984, he joined as an Assistant Professor with the Department of Electrical Engineering, HIT, where he has been a Professor since 1994, and the Dean of School of Electrical Engineering and Automation, from 2000 to 2010. He is currently the Vice President of HIT. His research interests include renewable energy generation technology, power quality mitigation, sensorless vector controlled motor drives, and high-performance servo system. He has authored and coauthored more than 600 technical papers.

Dr. Xu is an Associate Editor of the IEEE TRANSACTIONS ON INDUSTRIAL ELECTRONICS, the IEEE TRANSACTIONS ON POWER ELECTRONICS and the IEEE JOURNAL OF EMERGING AND SELECTED TOPICS IN POWER ELECTRONICS. He currently serves as Chairman of IEEE Harbin Section. He was the recipient of 2018 IEEE Industry Applications Society Outstanding Achievement Award.